Check for updates

Solar RRL
www.solar-rrl.com

Beyond Light-Trapping Benefits: The Effect of SiO_2 Nanoparticles in Bifacial Semitransparent Ultrathin Cu(In,Ga)Se_2 Solar Cells

Yong Li, Stefan W. Tabernig, Guanchao Yin, Albert Polman, and Martina Schmid**

Bifacial semitransparent ultrathin Cu(In,Ga)Se_2 solar cells (BSTUT CIGSe SCs) enable efficient usage of light and reduced raw material. By inserting the SiO_2 nanoparticles (NPs) at the CIGSe/back–contact interface, this work optimizes the performance of BSTUT SCs under front and especially rear illumination, which has not been studied much so far. For the SCs with NPs, the short-circuit current density increases by 4.1–4.4 mA cm^{-2} for front and by 6.4–7.4 mA cm^{-2} for rear illumination. In addition, a significantly improved fill factor for rear illumination highlights a benefit of the NPs beyond light trapping. A jet-like focusing behind the NPs is observed, which in this case leads to a higher field localization near the pn junction, joint with an enhanced carrier generation and separation. Furthermore, a thinner In_2O_3:Sn (ITO) back contact is noticed to be favorable for effective light trapping, whereas thicker ITO is preferred for higher open-circuit voltage. Overall, inserting NPs in BSTUT SCs is an effective and practical strategy to achieve a higher cost-to-efficiency ratio in photovoltaic device production. In our case, a maximum of 12.2% under front and 9.2% under rear illumination is achieved leading to a calculated bifacial efficiency of 15% for the ultrathin device.

1. Introduction

With carbon neutrality becoming a central request in economic development nowadays, green energy like photovoltaics (PV) stands in an increasingly prominent position.[1] Compared with silicon-based solar cells (SCs), polycrystalline thin-film SCs based on Cu(In,Ga)Se_2 (CIGSe) have many unique advantages such as smaller light-induced degradation and shorter energy payback time.[2–5] Those characteristics provide the CIGSe panels with a longer stable lifetime and lower fabrication cost. From the material point of view, because the defects in the chalcopyrite CIGSe act as effective doping, the error-tolerance toward defects introduced during the production process is high, which is advantageous for large-scale production.[6] In addition, the CIGSe bandgap E_g can be tuned by adjusting the Ga/(Ga + In) element ratio or by replacing In with Ga, Cu with Ag, and S with Se. Therefore, CIGSe can be flexible and applicable in tandem SCs.[7,8]

Among the CIGSe SC family, ultrathin CIGSe (<500 nm) has drawn more and more attention recently.[9–13] One major reason is, if light management was applied properly, the ultrathin CIGSe SCs show an equally high theoretical conversion efficiency (Eff) as the standard thick ones (≈2000 nm) while reducing the raw material consumption, especially of the rare metal indium.[14–16] In laboratory experiments, 15% record efficiency has been achieved on Mo substrates.[17] In the state-of-the-art PV performance, the biggest difference between the ultrathin and the standard thick SCs is the short-circuit current density j_{sc}.[5,17] The j_{sc} is 26.4 mA cm^{-2} for an absorber thickness of 500 nm and 39.6 mA cm^{-2} for an absorber thickness of 2 µm. The reason for the drop in j_{sc} is insufficient light absorption in the ultrathin CIGSe, which further induces high-parasitic absorption in the Mo layer, especially in the long-wavelength range.[18] On the one hand, various light-trapping strategies were developed to redirect and localize the light in the absorber, like nanoparticles (NPs) and reflective back mirrors.[19–22] On the other hand, if the ultrathin CIGSe was fabricated on a transparent back contact, the ultrathin CIGSe SCs become semitransparent, and the unabsorbed part of the light can be utilized in other ways.[9,13,23,24] Furthermore, semitransparent SCs have abundant application scenarios, for example, building-integrated PV, agrivoltaics, and vehicle-integrated PV. In addition, it is compatible with laser scribing in module fabrication.[25,26] Furthermore, bifacial SCs can exploit back-reflected light and thus enhance the efficiency. Given the earlier considerations, this work aims at improving the bifacial PV performance of bifacial semitransparent ultrathin CIGSe SCs (BSTUT CIGSe SCs) via SiO_2-NP light trapping.

Y. Li, M. Schmid
Faculty of Physics
University of Duisburg-Essen & CENIDE
47057 Duisburg, Germany
E-mail: martina.schmid@uni-due.de

S. W. Tabernig, A. Polman
Department for Sustainable Energy Materials
NWO-Institute AMOLF
1098 XG Amsterdam, The Netherlands

G. Yin
School of Materials Science and Engineering
Wuhan University of Technology
Wuhan 430070, China
E-mail: guanchao.yin@whut.edu.cn

The ORCID identification number(s) for the author(s) of this article can be found under https://doi.org/10.1002/solr.202200695.

DOI: 10.1002/solr.202200695

 © 2022 Wiley-VCH GmbH

Light trapping has been identified as a promising strategy to strengthen the efficiency of ultrathin SCs.[20] Lately, Collin et al. reviewed the theoretical and experimental progress of ultrathin SCs made by different materials (c-Si, CdTe, and CIGSe).[27] They highlighted how the extended optical path (from single-path absorption to the Lambertian scattering limit) enhances the j_{sc} of ultrathin SCs.[27] For an advanced description of light-trapping effects, Fan et al. theoretically divided the optical modes into four categories based on electromagnetic SC simulations: 1) Mie resonances, 2) low-quality-factor Fabry–Pérot standing-wave resonances, 3) guided resonances, and 4) diffracted modes.[19] By optimizing the near-field distribution of the optical modes in the absorber and the angular distribution of the differential scattering cross section, Schmid et al. compared different NP materials (metal, semiconductor, and dielectric),[28] sizes,[29] and positions (top and bottom)[30,31] in the ultrathin CIGSe SCs by simulations and experiments, which provides practical guidance for optimization. In terms of experiments, the light-trapping particles/layers have been inserted at different locations which proved beneficial for the PV performance of the SCs. For instance, a light-trapping layer can be added atop the ZnO as antireflection coating,[13] between CdS/CIGSe,[32] or at the CIGSe/back interface as a reflective mirror to harvest more photons.[22,33]

However, light trapping in BSTUT SCs has not gained much attention so far, especially under rear illumination, neither in simulations nor in experiments. Most of the light-trapping research focused on front illumination only, as an opaque back contact like Mo was presumed. Recently, we improved the front illumination open-circuit voltage (V_{oc}) of the ultrathin CIGSe SCs by optimizing the Na doping and by adjusting the ITO (In_2O_3:Sn) thickness to diminish the back contact potential barrier height E_h.[24,34] Instead of other materials (such as ZnO:Al and In_2O_3:F), we chose ITO as the back contact for BSTUT CIGSe SCs because ITO can tolerate high temperature necessary for the sequential CIGSe co-evaporation process. At this stage, it is tempting to add the SiO_2 NPs to further improve the j_{sc} of the BSTUT SCs and especially to explore the light-trapping effects under rear illumination. For the BSTUT SC operation under rear illumination, many questions are raised simultaneously, for example, how do the NPs trap the rear illumination light, and what effect has the reversed distribution of photogenerated carriers? For the first query, according to theoretical findings by Backman et al., NPs such as cylinders and spheres can scatter the incident light in the forward direction and form a photonic nanojet on the shadow side.[35,36] Yin et al. also observed the jet-like light-trapping effects when simulating the ultrathin CIGSe SCs under rear illumination.[18] However, whether the forward-scattering induced by the NPs is experimentally beneficial for the rear illuminated SCs will be verified in this work.

Our BSTUT CIGSe SC consists of ZnO/CdS/CIGSe/ITO/glass as shown in **Figure 1**a. Light incidence from the ZnO side will be referred to as front illumination and the case of light coming from the glass side will be referred to as rear illumination. In this contribution, we fabricate the SiO_2 NPs at the CIGSe/ITO interface on 100 and 300 nm ITO, typical thicknesses that were shown to be beneficial for front illumination in our previous work.[18,30,31,37,38] In particular, in Ref. [1], we have proven by simulations that for ultrathin CIGSe SCs with optimal SiO_2 NPs (size, height, and pitch), the j_{sc} can increase by 4.2 for front and 3.9 mA cm^{-2} for rear illumination (with an Ag front reflector). In the experiments of this article, the diameter, pitch, and height of the SiO_2 hemispheres were 380, 513, and 200 nm, respectively, as shown in Figure 1b, which followed our previous work.[31] Although those NP parameters do not exactly coincide with the predicted optimum in Ref. [1], they are close enough to the optimum to warrant the demonstration of bifacial light trapping. In the following, we will first compare the bifacial PV parameters of the BSTUT SCs with and without SiO_2 NPs to verify the light-trapping effects. Second, to clarify the j_{sc} enhancement mechanism, bifacial external quantum efficiency (EQE) and transmission/reflection (T/R) will be compared in detail. The influence of the ITO thickness will be discussed, and the light-trapping mechanism of the SiO_2 NPs under front and rear illumination will be examined in detail. In particular, extra electronic benefits of the SiO_2 NPs under rear illumination will be proposed. Finally, an overall conclusion of the light-trapping effects in BSTUT CIGSe SCs will be given.

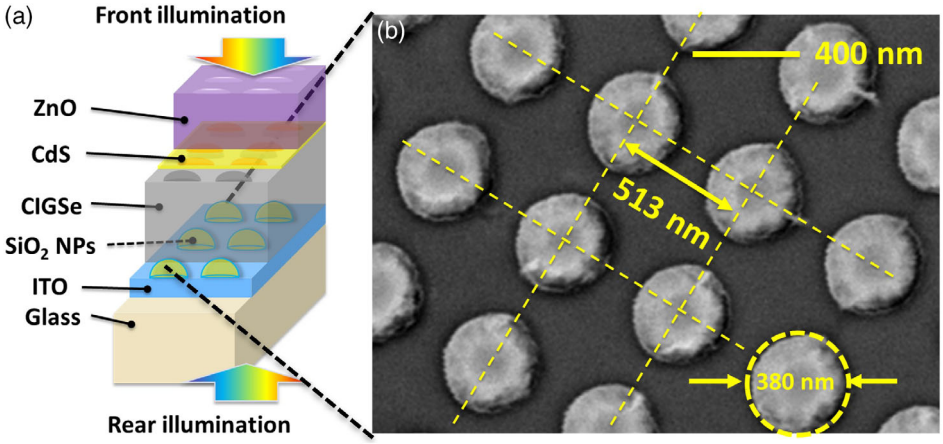

Figure 1. a) The position of the nanoparticles (NPs) in the ultrathin CIGSe solar cell (SC) with illumination options from front and rear and b) top view of the SiO_2 NPs.

© 2022 Wiley-VCH GmbH

2. Fabrication and Characterization

2.1. SiO_2 NP Fabrication

We used substrate conformal imprinting lithography to fabricate the SiO_2 NPs on ITO substrates.[31] First, we spin-coated a thin layer (280 nm) of polymethyl methacrylate (PMMA) onto the ITO substrates. Then, silica sol–gel was spin-coated on top of the PMMA and imprinted using a polydimethylsiloxane (PDMS) stamp. The patterned sol–gel layer was etched using reactive ion etching (RIE) with a mixture of CHF_3 and Ar, until a breakthrough in the PMMA was achieved. This was followed by an O_2 RIE etch to transfer the sol–gel pattern into the PMMA. Subsequently, 200 nm of SiO_2 were evaporated, filling up the hole features of the pattern. Followed by acetone lift-off, SiO_2 pillars were left on a clean ITO surface. The SiO_2 NPs have a height of 200 nm, a diameter of 380 nm, and a pitch of 513 nm, as shown in Figure S3, Supporting Information.

2.2. Ultrathin CIGSe SC Fabrication

The ITO layer was deposited on cleaned alkali-free Corning 7059 glass substrates by DC sputtering. 120 W sputtering power and 9 cm target-substrate distance were optimized values to achieve the best homogeneity and sputtering rate (2.5–2.7 Å s^{-1}). In the Ar atmosphere, the sputtering pressure was 7.5×10^{-4} mbar. The ITO thickness variation was realized by simply adjusting the time period of sputtering. After the SiO_2 NP deposition, the 100 nm (ITO-100) and the 300 nm ITO (ITO-300) reference substrates were put into the physical vapor deposition chamber along with the NP-patterned samples of ITO-100–SiO_2 and ITO-300–SiO_2 for the same batch of CIGSe absorber fabrication. The CIGSe layer was grown by the standard 3-stage co-evaporation process monitored by a laser light-scattering method. The co-evaporation went through a Cu-rich phase and ended with an overall Cu-poor content ratio. The substrate temperature for the first stage was set 410 °C, which was ramped up to 450 °C for the second and the third stage. Following was a Na postdeposition treatment with 2 mg of NaF in our case, which was conducted at 360 °C substrate temperature. Afterward, 60 nm CdS were coated by chemical bath deposition at 60 °C for 8 min. The front layers of 80 nm intrinsic ZnO (i-ZnO) and 300 nm ZnO:Al (AZO) were radio-frequency sputtered at a substrate temperature of 120 °C. Finally, the 10 nm Ni/2000 nm Al front contacts were deposited by thermal evaporation. In the end, the BSTUT SCs have the structure Al/Ni/AZO/i-ZnO/CdS/CIGSe/ITO/glass.

2.3. Characterization Methods

The ITO thickness was monitored by a calibrated quartz balance installed next to the substrates. The thickness and composition of the CIGSe layer were determined by X-ray fluorescence spectroscopy, and they were found to be 468 nm thickness, CGI (Cu/(Ga + In)) of 0.83, and GGI (Ga/(Ga + In)) of 0.33. Total T/R under front and rear illumination was measured by a Perkin Elmer 1050 UV–vis–NIR spectrometer with an integrating sphere. Front and rear current–voltage (I–V) properties were evaluated by a standard AAA solar simulator at 23 °C on a black-painted sample holder. Bifacial EQE was characterized by a home-built system with a Xe and a He lamp on black paper to avoid reflection from the sample holder. Before the BSTUT SC measurements, the EQE was calibrated by Si and GaAs reference SCs.

3. Results and Discussion

Table 1 summarizes the front/rear PV parameters of the BSTUT SCs with/without SiO_2 NPs along with the equivalent current density j_{EQE} integrated from EQE results, and **Figure 2** plots the evolution trends. For simplicity, ITO-100 represents 100 nm thick ITO and ITO-100–SiO_2 represents 100 nm thick ITO textured with SiO_2 NPs. The abbreviations of ITO-300 and ITO-300–SiO_2 are the same correspondingly.

3.1. Front Illumination

ITO-100–SiO_2 shows 4.4 mA cm^{-2} j_{sc} increase compared with ITO-100, which is close to the simulated value of 4.2 mA cm^{-2}.[18] Meanwhile, ITO-300–SiO_2 shows 4.1 mA cm^{-2} j_{sc} increment, also close to the simulation prediction. It is worth mentioning that 200 nm ITO was used in our previous simulation, and that the pattern dimensions are not exactly the same. ITO-100–SiO_2 shows 0.3 mA cm^{-2} higher j_{sc} than ITO-300–SiO_2 because thinner ITO means a shorter optical path for the light reflected from the ITO/glass interface, thus less parasitic absorption loss.[18] The V_{oc} is increased by 5 mV on ITO-100 and by 10 mV on ITO-300 with SiO_2 NPs. This is attributed to the NPs' light-trapping effects again, as the V_{oc} is related to the j_{sc} by

$$V_{oc} = \frac{nkT}{q} \ln\left(\frac{j_{sc}}{j_0} + 1\right) \quad (1)$$

where n is the diode ideality factor, kT/q is the thermal voltage (0.0259 V at room temperature), and j_0 is the dark saturation current density. If we set n to an extreme value of 2 for all cells,[31] j_0 to 4E-3 mA cm^{-2} for ITO-100 and to 2.5E-3 mA cm^{-2} for ITO-300, the V_{oc} gain of the SiO_2 patterned cells can be closely correlated to the j_{sc} increase via Equation (1).[31] ITO-300 shows

Table 1. Front and rear PV parameters of ultrathin CIGSe SCs with/without SiO_2 NPs at the CIGSe/back contact. ITO-100 represents an ITO thickness of 100 nm and ITO-100–SiO_2 represents the 100 nm ITO is textured with SiO_2 NPs. In the same way, ITO-300 and ITO-300–SiO_2 have 300 nm ITO. The suffix "R" means the rear PV parameters.

		j_{sc} [mA cm^{-2}]	j_{EQE} [mA cm^{-2}]	V_{oc} [mV]	FF [%]	Eff [%]	Best Eff [%]
Front illumination	ITO-100	26.7	26.4	579.3	57.4	8.9	9.8
	ITO-100–SiO_2	31.1	31.6	584.2	55.3	10.1	10.8
	ITO-300	26.7	26.2	598.2	60.0	9.6	10.2
	ITO-300–SiO_2	30.8	31.0	608.1	60.6	11.3	12.2
Rear illumination	ITO-100R	21.3	20.5	554.5	37.2	4.4	4.6
	ITO-100–SiO_2R	28.7	28.2	561.5	43.5	7.0	7.8
	ITO-300R	19.8	20.2	563.5	36.9	4.1	4.8
	ITO-300–SiO_2R	26.2	26.1	583.5	55.9	8.5	9.2

© 2022 Wiley-VCH GmbH

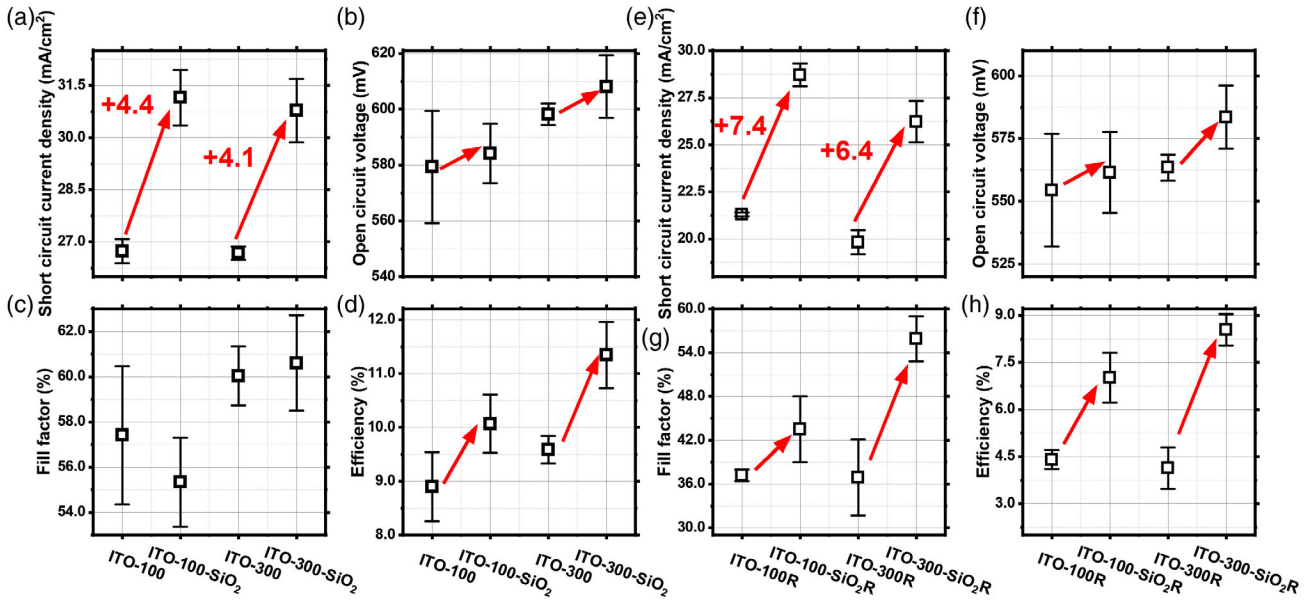

Figure 2. a–d) Experimental photovoltaic (PV) parameters under front illumination before and after SiO_2 NPs insertion. e–h) Corresponding PV parameters under rear illumination. The error bars represent the standard deviation of the PV performance.

higher V_{oc} and lower j_0 than ITO-100 due to the so-called Burstein–Moss (B–M) shift in the ITO layer that diminishes the back contact barrier height E_h at the CIGSe/ITO interface.[24] The fill factor (*FF*) shows a tiny fluctuation, as for ITO-100–SiO_2 it decreases by 2.1%, whereas for ITO-300–SiO_2 it increases by 0.6% compared with their references. Actually, we repeated the same comparative experiments three times, as shown in Figure S1 and Table S1, Supporting Information. The overall trend is clear: both V_{oc} and j_{sc} are enhanced by the SiO_2 NPs, only *FF* drops slightly. From the device point of view, the *FF* decrease can be attributed to the series resistance induced by the SiO_2 NPs, as the SiO_2 NPs are isolators with higher electrical resistivity. In terms of efficiency Eff, the NPs enhance it by 1.2% on 100 nm and by 1.7% on 300 nm ITO, demonstrating effective light trapping under front illumination.

To better understand the mechanism of the j_{sc} gain, EQE measurements were employed to characterize representative cells of each sample. Because the EQE measurements do not depend on the area of the cells, the current density j_{EQE} integrated from EQE is considered as an independent method to cross-check the j_{sc} results measured by (*I*–*V*) characteristics.[39] The j_{EQE} shows consistency with the j_{sc} as provided in Table 1. **Figure 3** compares the samples of different ITO thicknesses with and without NPs. For an improved understanding of differences in EQE (black line), it is helpful to compare it directly with the *T*/*R*, shown in red and green, respectively.

First, we compare ITO-100 and ITO-300 to see the influence of the ITO thickness, as shown in Figure 3a. In the short-wavelength range from 300 to 510 nm where the window layers (ZnO:Al/i-ZnO/CdS) show severe absorption, the EQE plots overlap because the window layers are identical. In the range from 510 to 990 nm, a larger variation in EQE is visible originating from Fabry–Pérot interferences caused by the ITO thickness change.[37] Above 990 nm, ITO-100 shows higher EQE because thinner ITO induces less parasitic absorption, being most pronounced in the long-wavelength range.[40] For the 100 nm thick ITO, more light can be reflected into the absorber from the ITO/glass interface. Due to the reduced parasitic absorption, ITO-100 also shows higher transmission as indicated by the red solid line in Figure 3a. The EQE cut-off wavelength is the same for ITO-100 and ITO-300 as it relates to the absorber bandgap E_g, which is 1.12 eV in both cases.

Figure 3b illustrates samples with 100 nm ITO with and without NPs. ITO-100–SiO_2 shows overall higher EQE, revealing excellent light-trapping effects of the SiO_2 NPs. It can directly be correlated with the lowered *T*/*R*, as shown by the red and green short dashed lines. At wavelengths of 1120 and 1180 nm, two pronounced EQE peaks are particularly interesting. According to our previous optical simulations study, waveguide modes induced by the SiO_2 NPs are responsible for them.[31] From 500 nm onwards, ITO-100–SiO_2 reveals a lower transmission than ITO-100. A single valley and double valley can be distinguished at 1085 and 1280 nm in transmission, respectively, which is caused by the scattering of the NPs.[18] In short, the SiO_2 NPs effectively diminish *T*/*R* and enhance the light absorption in the BSTUT SCs via improved light trapping.

Similar to ITO-100–SiO_2, ITO-300–SiO_2 shows overall higher EQE and lower transmission, see Figure 3c. From 510 nm on, the EQE of ITO-300–SiO_2 is strengthened because the NPs reduce the overall transmission and partly diminish the reflection. Comparing ITO-100–SiO_2 and ITO-300–SiO_2 (Figure 3d), we notice that the EQE overlaps in the range from 300 to 750 nm wavelength. The reason can originate from the dominating effect of window layer parasitic absorption which is identical for both cases as well as from the main CIGSe absorption. From 750 nm on, ITO-100–SiO_2 prevails in EQE, suggesting that the NPs work better on 100 nm ITO, especially in the long-wavelength range, where the ITO parasitic absorption is non-negligible. The EQE

© 2022 Wiley-VCH GmbH

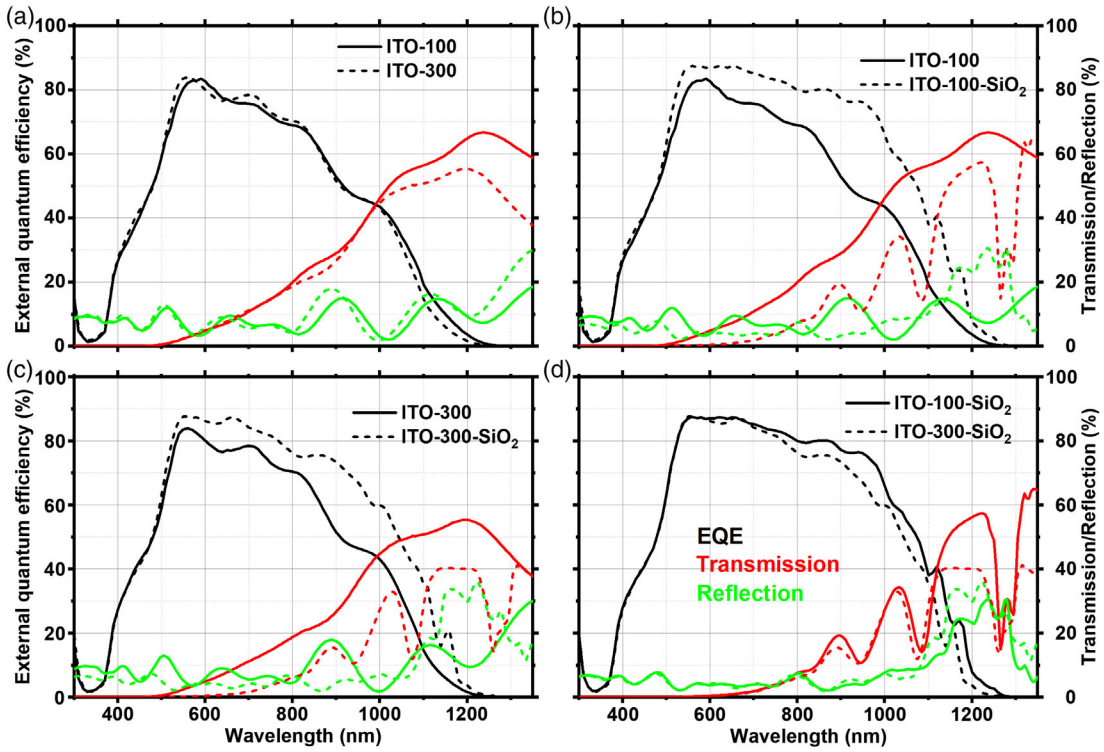

Figure 3. Ultrathin CIGSe SCs on 100 or 300 nm ITO back contact without or with the integration of SiO_2 NPs under front illumination, in which the measured external quantum efficiency (EQE), transmission, and reflection are shown in black, red, and green, respectively. a) compares ITO-100 with ITO-300, b) compares ITO-100-SiO_2 with the reference ITO-100, c) compares ITO-300-SiO_2 with the reference ITO-300, and d) compares ITO-300-SiO_2 with ITO-100-SiO_2.

shows two peaks (1120 and 1180 nm) for ITO-100–SiO_2, where ITO-300–SiO_2 shows one at 1160 nm and a steep feature at 1100 nm. The stronger parasitic absorption brought by the thicker ITO can also be seen in the transmission line being significantly lower and flattened in the long-wavelength range. With NPs, the difference in ITO parasitic absorption coming from its thickness change appears intensified. This may be attributed to the jet-like forward-scattering effect of the NPs, which concentrates the long-wavelength light inside the ITO and increases the parasitic absorption there.

3.2. Rear Illumination

When it comes to rear illumination, we notice that the SiO_2 NPs improve all the PV parameters on both ITO thicknesses, as plotted in Figure 2e–h. Impressively, the j_{sc} is enhanced by 7.4 mA cm^{-2} on 100 nm ITO and by 6.4 mA cm^{-2} on 300 nm ITO. This is much higher than the front j_{sc} gain of 4.2 mA cm^{-2}. It may imply that the NPs are trapping the light in a different regime under rear illumination. Optical simulations suggested that the highest electric field intensity locates closer to the space charge region (SCR) of the SC, where the photogenerated carriers can be effectively separated and collected, hence ensuring that most generated charges contribute to j_{sc}. Judging by the *FF* increase of the SCs, the SiO_2 NPs have effectively improved the collection efficiency of photogenerated carriers under rear illumination.[41] The V_{oc} also increases by 17 and 20 mV on 100 and 300 nm ITO, respectively, which is close to the enhancement estimated from Equation (1), if we again set n to 2 (and $kT/q = 0.0259$ V) for all cells and j_0 to 5E-3 mA cm^{-2} for ITO-100 and 3.5E-3 mA cm^{-2} for ITO-300. The consistency implies the V_{oc} gain mainly originates from the light-trapping effect. Similar to the front illumination, the V_{oc} of ITO-300 is higher than ITO-100 because of the B–M shift in the ITO; equally, the j_{sc} of ITO-300 is slightly lower than that of ITO-100 because of the higher parasitic absorption losses.[24] So is the case for j_{sc} of ITO-300–SiO_2 and ITO-100–SiO_2. The Eff is boosted from 4.4% to 7.0% on 100 nm ITO and from 4.1% to 8.5% on 300 nm ITO, corresponding to 59% and 107% relative efficiency enhancement.

In general, the major factors influencing the EQE in the short-wavelength range are the corresponding front layers and their E_g, whereas in the long-wavelength range, the absorption of free-charge carriers in the front or rear layers is influential. **Figure 4** compares the EQE aligned with T/R under rear illumination (appendix R represents the rear illumination). In this case, it is the ITO parasitic absorption that dominates the loss in the short-wavelength range, replacing the ZnO/CdS layers which dictate the optical loss behavior under front illumination.[24] For this reason, a bump at around 370 nm can be seen in the rear illumination EQE, where there is none under front illumination. In Figure 4a, the black short dash shows a higher EQE for ITO-300R than for ITO-100R in the wavelength range from 340 to 520 nm, the reason being a wider E_g for 300 nm ITO than for 100 nm.[40,42] In addition, ITO-300R shows a lower EQE in the

© 2022 Wiley-VCH GmbH

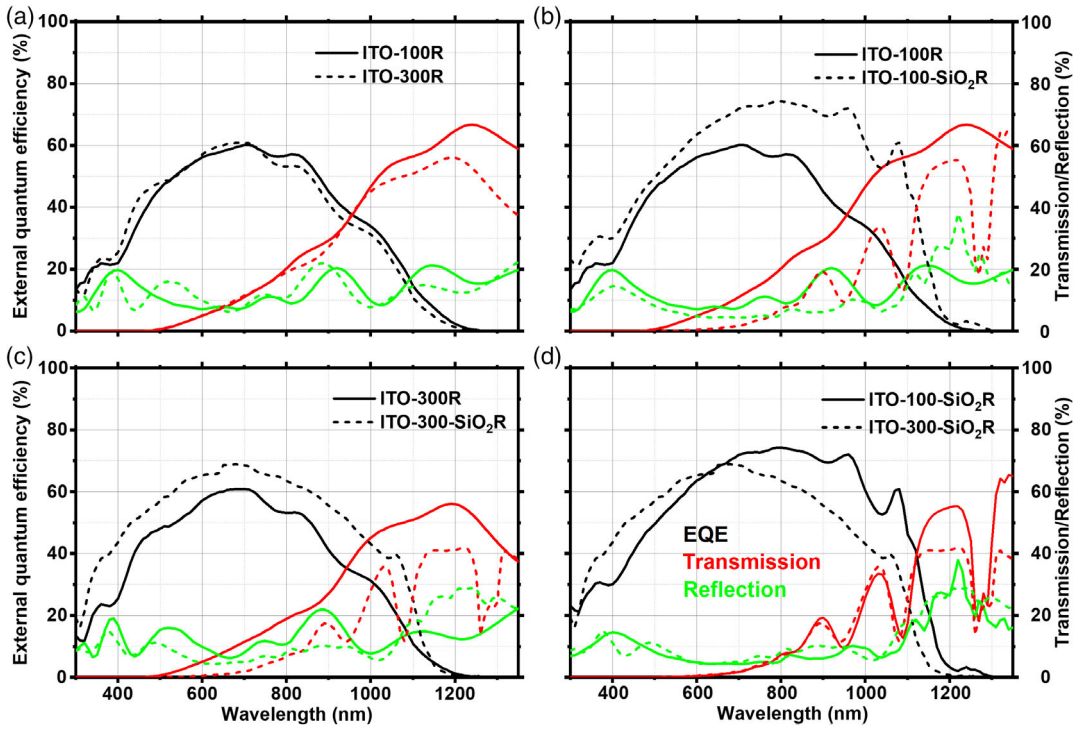

Figure 4. Ultrathin CIGSe SCs on 100 or 300 nm ITO back contact without or with the integration of SiO_2 NPs under rear illumination, in which the measured external quantum efficiency (EQE), transmission, and reflection are shown in black, red, and green, respectively. a) compares ITO-100R with ITO-300R, b) compares ITO-100–SiO_2R with the reference ITO-100R, c) compares ITO-300–SiO_2R with the reference ITO-300R, and d) compares ITO-300–SiO_2R with ITO-100–SiO_2R.

range from 730 to 1260 nm because the increased ITO parasitic absorption becomes dominant for long wavelengths. This is confirmed in T/R from 1050 to 1350 nm wavelength, as ITO-300R shows lower transmission and reflection thus overall higher parasitic absorption. It is worth mentioning that Fabry–Pérot interferences can also be seen in reflection from 300 to 650 nm wavelength: while one peak is found for ITO-100R, there are three for ITO-300R, which is related to the thickness variation of the ITO in the multilayers system.

In Figure 4b, ITO-100–SiO_2R shows an overall higher EQE than ITO-100R. In the long-wavelength range, the absorption might be enhanced by the jet-like forward scattering of the NPs and stronger optical scattering in general.[18,43] At 960 and 1080 nm, two pronounced EQE peaks show up, corresponding to waveguide modes originating from the regularly arranged SiO_2 NPs.[31] T/R is effectively suppressed, as shown by the red and green short dashed lines. At around 400 nm, both ITO-100R and ITO-100–SiO_2R exhibit the thickness-dependent identical Fabry–Pérot interference peak in reflection. On 300 nm ITO (Figure 4c), the insertion of SiO_2 NPs may have tuned the Fabry–Pérot interferences of the multilayer SCs, as the reflection interference peaks at 380 and 520 nm appears shifted. Overall, the transmission is suppressed by the NPs for ITO-300–SiO_2R; hence, the EQE is enhanced enormously.

Comparing ITO-100–SiO_2R with ITO-300–SiO_2R, as shown in Figure 4d, ITO-300–SiO_2R exhibits higher EQE in the wavelength range from 300 to 630 nm. This can be understood because ITO-300–SiO_2 has a wider E_g of ITO due to the B–M shift.[24] However, ITO-100–SiO_2R shows much higher EQE in the range from 670 to 1300 nm, which implies that optical scattering, dominant in the long-wavelength range, can work more efficiently for light trapping with the higher transmission through the thinner ITO. Hence, the waveguide-mode enhancement at 1080 nm is much stronger on ITO-100–SiO_2R than on ITO-300–SiO_2R, and a peak at 960 nm can only be recognized on ITO-100–SiO_2R. Overall, ITO-100–SiO2R achieves the highest j_{EQE} of 28.2 mA cm^{-2}. In addition, the reflection in the wavelength range from 300–750 nm is dominated by Fabry–Pérot interferences alike in Figure 4a. In the wavelength range from 600 to 1350 nm, transmission valleys aligned with each other are attributed to the NPs having the same height, size, and pitch, which decided the corresponding wavelengths of enhanced absorption.

3.3. Front and Rear Illumination Comparison

After the detailed electrical and optical comparison, we notice that the light-trapping mechanism of the same SiO_2 NPs is different when the illumination direction is reversed, and the j_{sc} enhancement under rear illumination is much higher than under front illumination. To better see the differences in mechanism, and the deviation between simulation and experiments, **Figure 5**a shows the forward-scattering light-trapping effects under front (green) and rear (blue) illumination, which was vividly coined as jet-like by Yin et al.[18] The electric field distribution of the jet-like profile is similar to the so-called photonic nanojets, even though the shape of the NPs is hemispherical for jet-like and spherical for nanojets. As shown in Figure 5b, it is a narrow,

© 2022 Wiley-VCH GmbH

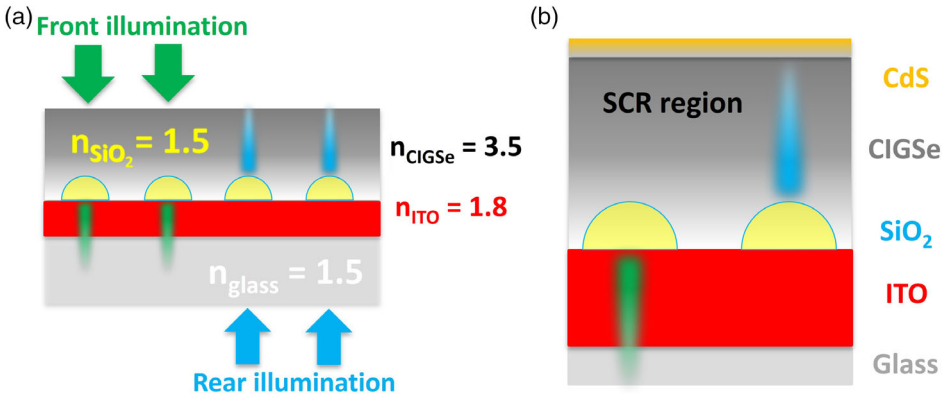

Figure 5. a) Jet-like electrical field distribution in the bifacial semitransparent ultrathin BSTUT SCs under (bifacial) illumination and b) the orientation of the jet-like electric field with respect to the space charge region (SCR) of the SC under front and rear illumination. Green color represents the electric field distribution under front illumination, and blue color corresponds to the rear illumination. The wavelength of the illumination is around 800 nm.

high-intensity, and nonevanescent light beam that emerges from the shadow-side surface of an illuminated NP.[36] The size and shape of the NPs[29] as well as the refractive index of the NP versus the one of the medium can influence the shape of the jet-like electric field distribution.[28] Yet, under different illumination directions, the most critical point is the location of the jet with respect to the SCR. When the ultrathin SC is working under front illumination, the jet-like light focus is directed into the ITO layer, which cannot be utilized by the SC. In this case, the NPs enhance the absorption via light scattering and enhanced reflectivity from the SiO_2/CIGSe interface.[18] When the illumination is reverted to the rear side, however, the SiO_2 NPs will generate the jet-like electrical field and enhance the absorption inside the device. In addition, the concentrated electric field is directed toward the SCR of the SC, where the recombination is much smaller than at the CIGSe/ITO interface. It brings extra electronic benefits to the carrier extraction in the SC, and it is significant because the SCR width of the ultrathin CIGSe SC is close to the thickness of the absorber.[34] Those benefits are similar to the quantum dot SCs on nanopatterned substrates, in which the light-trapping geometry shifted the optical hot spot which affected the collection efficiency of the photogenerated carriers. The improved rear *FF* of the SCs with NPs also suggests that the photogenerated carriers are extracted more efficiently.[41,44] For the deviation in rear j_{sc} gain between the simulations and experiments, it shall be noted that the reference sample in our early simulations used an Ag mirror on the front side of the cell, which is not the case in the experiments presented here.[18] The even higher gain in rear j_{sc} than in front j_{sc} is suggesting extra advantages of improved collection efficiency in addition to the light-trapping effects for SiO_2 NPs under rear illumination. Our experimental findings reveal the potential of the SiO_2 NPs in BSTUT SCs, especially under rear illumination, which is equally important to be considered for bifacial applications.

4. Conclusions

Compared with the CIGSe SCs of standard thickness (≈2000 nm), the BSTUT SCs suffer from a low j_{sc} because of insufficient light absorption. Appropriate light management is essential, as it can effectively enhance the light absorption in the ultrathin absorber. Combining the EQE with the *T*/*R* characteristics of the BSTUT SCs, this work comparatively studies the influences of SiO_2 NP integration underneath a 468 nm thick CIGSe absorber along with variations of ITO back contact thickness. The PV performance shows that the insertion of NPs at the CIGSe/ITO interface is beneficial for the SCs on both 100 and 300 nm thick ITO substrates. With SiO_2 NPs, the front illumination j_{sc} is increased by 4.1–4.4 mA cm^{-2} consistent with the simulation prediction of 4.2 mA cm^{-2}. The average front Eff increases from 8.9% to 10.1% on 100 nm ITO and from 9.6% to 11.3% on 300 nm ITO. The rear illumination j_{sc} is enhanced by 6.4–7.4 mA cm^{-2}, which is higher than the front j_{sc} gain, suggesting that the SiO_2 NPs not only enhance the light absorption but also contribute to the collection efficiency of the photogenerated carriers. Unlike the front *FF*, the rear *FF* is enhanced for the samples with SiO_2 NPs, which confirms an improved carrier extraction under rear illumination. The average rear Eff increases from 4.4% to 7.0% and from 4.1% to 8.5% on 100 and 300 nm ITO, respectively, corresponding to 59% and 107% relative increase. The bifacial illumination Eff would be 15.0% if we sum up 100% front and 30% rear Eff of our best SC,[9] which is close to the 15.2% record of the Mo-based ultrathin CIGSe SCs.[17] Compared with the flat reference samples, the SiO_2 NPs induce waveguide modes and enhance front and rear absorption in the ultrathin CIGSe layer. The NPs also induce jet-like forward scattering, which further enhances the light localization inside the absorber layer and increases the collection efficiency of photogenerated carriers under rear illumination. The thicker ITO casts higher parasitic absorption in the long-wavelength range but brings higher rear illumination EQE in the short-wavelength range and higher front/rear V_{oc} due to the wider E_g caused by the B–M shift. For the SiO_2 NPs, those experimental results verify the light-trapping theory under front and rear illumination, which reveals a promising prospect in bifacial semitransparent SCs.

Supporting Information

Supporting Information is available from the Wiley Online Library or from the author.

© 2022 Wiley-VCH GmbH

Acknowledgements

All authors would like to express their sincere gratitude to Tristan Köhler and Klaus Pärschke for technical support and to Jan Lucaßen, Yao Gao, and Setareh Sedaghat for fruitful discussions and revisions. The XRF measurements were performed on an instrument funded by the Deutsche Forschungsgemeinschaft (DFG, German Research Foundation) – INST 20876/324-1 FUGG and are acknowledged as follows: "Gefördert durch die Deutsche Forschungsgemeinschaft (DFG) – Projektnummer INST 20876/324-1 FUGG". Y.L. receives subsidy from the Chinese Scholarship Committee and a Graduation Grant from the Duisburg-Essen University. G.Y. is funded by the National Natural Science Foundation of China (NSFC, 51802240). This work was performed in part at the NSW Node of the Australian National Fabrication Facility (ANFF). The authors acknowledge the facilities and the scientific and technical assistance of Microscopy Australia at the Electron Microscope Unit (EMU) within the Mark Wainwright Analytical Centre (MWAC) at UNSW Sydney. This work is part of the research program of the Dutch Research Council (NWO).

Conflicts of Interest

The authors declare no conflict of interest.

Author Contributions

Y.L.: conducted the SC fabrication and characterization and drafted the manuscript; S.W.T.: performed the SiO_2 NP fabrication and contributed with constructive discussion and revision; G.Y. and A.P.: contributed supervision; M.S. contributed supervision and revision.

Data Availability Statement

The data that support the findings of this study are available from the corresponding author upon reasonable request.

Keywords

bifacial solar cells, light trapping, semitransparent solar cells, SiO_2 nanoparticles, ultrathin CIGSe solar cells

Received: July 29, 2022
Revised: September 2, 2022
Published online:

[1] https://www.bp.com/en/global/corporate/energy-economics/statistical-review-of-world-energy.html (accessed: January 2021) **2021**.
[2] D. Abou-Ras, S. Wagner, B. J. Stanbery, H. Schock, R. Scheer, L. Stolt, S. Siebentritt, D. Lincot, C. Eberspacher, K. Kushiya, A. N. Tiwari, *Thin Solid Films* **2017**, *633*, 2.
[3] M. Ochoa, S. Buecheler, A. N. Tiwari, R. Carron. *Energy Environ. Sci.* **2020**, *12*, 2047.
[4] J. Yang, D. S. Chen, F. Xu, Z. Q. Ma, *Sol. Energy* **2013**, *98*, 415.
[5] M. Nakamura, K. Yamaguchi, Y. Kimoto, Y. Yasaki, T. Kato, H. Sugimoto, *IEEE J. Photovoltaics* **2019**, *9*, 1863.
[6] S. B. Zhang, S.-H. Wei, A. Zunger, *Phys. Rev. B* **1998**, *57*, 9642.
[7] J. Keller, N. S. Nilsson, A. Aijaz, L. Riekehr, T. Kubart, M. Edoff, T. Törndahl, *Prog. Photovoltaics* **2018**, *26*, 159.
[8] M. Saifullah, S. Ahn, J. Gwak, S. Ahn, K. Kim, J. Cho, J. H. Park, Y. J. Eo, A. Cho, J. Yoo, J. H. Yun, *J. Mater. Chem. A* **2016**, *27*, 10542.
[9] D. Kim, S. S. Shin, S. M. Lee, J. Cho, J. H. Yun, H. S. Lee, J. H. Park, *Adv. Funct. Mater.* **2020**, *30*, 2001775.
[10] M. Saifullah, J. Gwakab, J. H. Yun, *J. Mater. Chem. A* **2016**, *22*, 8512.
[11] M. Saifullah, S. Rasool, S. Ahn, K. Kim, J. Cho, J. Yoo, W. S. Shin, J. H. Yun, J. H. Park. *ACS Appl. Mater. Interfaces* **2019**, *11*, 655.
[12] K. Kima, W. N. Shafarmanb, *Nano Energy* **2016**, *30*, 488.
[13] M. J. Shin, A. Lee, A. Cho, K. Kim, S. K. Ahn, J. H. Park, J. Yoo, J. H. Yun, J. Gwak, D. Shin, I. Jeong, J. Cho, *Nano Energy* **2021**, *82*, 105729.
[14] P. Reinhard, F. Pianezzi, L. Kranz, S. Nishiwaki, A. Chirilă, S. Buecheler, A. N. Tiwari, *Prog. Photovoltaics* **2015**, *23*, 281.
[15] M. Gloeckler, J. R. Sites, *J. Appl. Phys.* **2005**, *98*, 103703.
[16] G. Yin, V. Brackmann, V. Hoffmann, M. Schmid, *Sol. Energy Mater. Sol. Cells* **2015**, *132*, 142.
[17] L. M. Mansfield, A. Kanevce, S. P. Harvey, K. Bowers, C. Beall, S. Glynn, I. L. Repins, *Prog. Photovoltaics* **2018**, *26*, 949.
[18] G. Yin, P. Manley, M. Schmid, *Sol. Energy* **2018**, *163*, 443.
[19] M. L. Brongersma, Y. Cui, S. Fan, *Nat. Mater.* **2014**, *13*, 451.
[20] M. Schmid. *Semicond. Sci. Technol.* **2017**, *32*, 043003.
[21] B. Bissig, R. Carron, L. Greuter, S. Nishiwaki, E. Avancini, C. Andres, T. Feurer, S. Buecheler, A. N. Tiwari, *Prog. Photovoltaics* **2018**, *26*, 894.
[22] L. Gouillart, A. Cattoni, W. Chen, J. Goffard, L. Riekehr, J. Keller, M. Jubault, N. Naghavi, M. Edoff, S. Collin, *Prog. Photovoltaics* **2020**, *29*, 212.
[23] J. Keller, W. Chen, L. Riekehr, T. Kubart, T. Törndahl, M. Edoff, *Prog. Photovoltaics* **2018**, *26*, 846.
[24] Y. Li, G. Yin, M. Schmid, *Sol. Energy Mater. Sol. Cells* **2022**, *234*, 111431.
[25] https://www.ise.fraunhofer.de/en/business-areas/photovoltaics/photovoltaic-modules-and-power-plants/integrated-photovoltaics/agrivoltaics.html (accessed: December 2021).
[26] S. Kuk, Z. Wang, S. Fu, T. Zhang, Y. Y. Yu, J. Choi, J. Jeong, D. J. Hwang, *Appl. Phys. Lett.* **2018**, *112*, 134102.
[27] I. Massiot, A. Cattoni, S. Collin, *Nat. Energy* **2020**, *12*, 959.
[28] M. Schmid, P. Andrae, P. Manley, *Nanoscale Res. Lett.* **2014**, *9*, 11.
[29] M. Schmid, P. Manley, *J. Photonics Energy* **2014**, *5*, 057003.
[30] G. Yin, P. Manley, M. Schmid, *Sol. Energy Mater. Sol. Cells* **2016**, *153*, 124.
[31] G. Yin, M. W. Knight, M. Lare, M. M. S. Garcia, A. Polman, M. Schmid, *Adv. Opt. Mater.* **2017**, *5*, 1600637.
[32] S. Garud, N. Gampa, T. G. Allen, R. Kotipalli, D. Flandre, M. Batuk, J. Hadermann, M. Meuris, J. Poortmans, A. Smets, B. Vermang, *Phys. Status Solidi A* **2018**, *215*, 1700826.
[33] T. Schneider, J. Tröndle, B. Fuhrmann, F. Syrowatka, A. Sprafke, R. Scheer, *Sol. RRL* **2020**, *4*, 2000295.
[34] Y. Li, G. Yin, Y. Gao, T. Köhler, J. Lucaßen, M. Schmid, *Sol. Energy Mater. Sol. Cells* **2021**, *223*, 110969.
[35] Z. Chen, A. Taflove, *Opt. Express* **2004**, *12*, 1214.
[36] A. Heifetz, S. Kong, A. V. Sahakian, A. Taflove, V. Backman, *Comput. Theor. Nanosci.* **2009**, *6*, 1979.
[37] C. Lare, G. Yin, A. Polman, M. Schmid. *ACS Nano* **2015**, *9*, 9603.
[38] G. Yin, M. Song, S. Duan, P. Manley, D. Greiner, C. A. Kaufmann, M. Schmid, *ACS Appl. Mater. Interfaces* **2016**, *8*, 31646.
[39] S. S. Hegedus, W. N. Shafarman, *Prog. Photovoltaics* **2004**, *12*, 155.
[40] H. Kim, J. S. Horwitz, G. Kushto, A. Pique, Z. H. Kafafi, C. M. Gilmore, D. B. Chrise. *J. Appl. Phys.* **2000**, *88*, 6021.
[41] S. W. Tabernig, L. Yuan, A. Cordaro, Z. L. Teh, Y. Gao, R. Patterson, A. Pusch, S. Huang, A. Polman. *ACS Nano* **2022**, *16*, https://doi.org/10.1021/acsnano.1c11330.
[42] Y. Sato, T. Ashida, N. Oka, Y. Shigesato, *Appl. Phys. Express* **2010**, *3*, 061101.
[43] M. Schmid, P. Manley, A. Ott, M. Song, G. Yin. *J. Mater. Res.* **2016**, *31*, 3273.
[44] S. W. Tabernig, L. Yuan, Y. Gao, Z. Teh, C. E. A. Cordaro, *48th IEEE Photovoltaic Specialists Conf.*, New York **2021**.

© 2022 Wiley-VCH GmbH